*Journal of Sound and Vibration* (2001) **239**(4), 819–848
doi:10.1006/jsvi.2000.3218, available online at http://www.idealibrary.com on IDEAL®

# SHEAR LAYER REFRACTION CORRECTIONS FOR OFF-AXIS SOURCES IN A JET FLOW†

C. L. Morfey and P. F. Joseph

*Institute of Sound and Vibration Research, University of Southampton, Southampton SO17 1BJ, England, E-mail: clm@isvr.soton.ac.uk*

(*Accepted* 28 *June* 2000)

A set of equations is derived for converting acoustic measurements taken in a free-jet flight simulation facility, such as the U.K. Noise Test Facility at Pyestock or the French CEPRA-19 wind tunnel at Saclay, to equivalent farfield flight conditions. The equations are based on the high-frequency geometrical acoustics approximation, whose application in the present context was justified in early studies by Morfey and Tester in 1977 and by Amiet in 1978. However, the present work differs by allowing the source to be positioned off the jet centreline, anywhere within the flight stream. The flight stream jet is modelled as an axisymmetric parallel shear flow, with a shear layer thickness which is small compared with the jet diameter. The model also permits the microphone to be located anywhere outside the flow, arbitrarily close to the open jet. The consequences of off-axis source location are illustrated by numerical calculations.



## 1. INTRODUCTION

### 1.1. BACKGROUND

At the design stage of any new civil aircraft it is important to predict the noise it will produce, particularly at takeoff and landing. A complicating factor is the reflection or scattering of exhaust noise from the airframe structure. These so-called *installation effects* are currently not well understood, so their presence introduces some uncertainty into flyover noise predictions. Moreover, they often increase the noise levels on the ground. Specifically, the static-to-flight noise reductions predicted from flight simulation tests on an isolated exhaust system are not realized on the installed engine.

There is a serious difficulty in isolating installation effects from full-scale tests alone. The reason is that noise measurements at full scale are normally limited to two conditions: *static*, with a bare engine on a test stand, and *in flight*, with a fully installed engine in an aircraft. In this situation it is impossible to decide how much of the difference in noise is due to flight effects, and how much to installation effects.

However by testing at model scale, in a flight simulation facility such as that at DERA (Pyestock, U.K.) or the CEPRA-19 wind tunnel (Saclay, France), a four-way comparison of static and in-flight noise from uninstalled and installed exhaust systems becomes feasible. The open-jet type of facility, in which measurements are taken outside the flight simulation stream, requires that the data be adjusted for amplitude, frequency and angle of observation

† An abbreviated version of this paper was presented by the second author at the first CEAS-ASC Workshop on Wind Tunnel Testing in Aeroacoustics (DNW, Noordostpolder, The Netherlands, 5–6 November 1997).
This paper is dedicated to Emeritus Professor Philip Doak on the occasion of his 80th birthday.

0022-460X/01/040819 + 30 $35.00/0 

in order to obtain sound pressure levels that are equivalent to flyover measurements made near the ground in the far field. In what follows, we refer to these data adjustments as "shear-layer corrections". Their calculation for off-axis sources is the subject of the present paper.

### 1.2. CALCULATION OF SHEAR-LAYER CORRECTIONS VIA GEOMETRICAL ACOUSTICS

A comparison is presented in reference [1] between the standard geometrical acoustics (GA) shear layer correction procedure and a wave-theory numerical calculation for on-axis sources in a round jet, using realistic ratios of shear-layer thickness ($\delta$) to acoustic wavelength ($\lambda_{ac}$); it shows agreement within typically 0·3 dB between the two transmitted pressure levels, even for single-frequency sources. Similar conclusions are reached in reference [2], using a two-dimensional geometry for the comparisons. For finite-bandwidth data (e.g., 1/3-octave) the agreement will be closer still.

Since the GA approximation provides closed-form analytical results for an axisymmetric plug flow, it has been adopted for the present study. An alternative to the analytical approach developed below would be to use the equations developed in references [3, 4] for numerical solution of the ray equations in a mean flow field, and to evaluate each specific flow and source geometry as required, using a suitable code. The numerical approach offers flexibility in the choice of flow fields, with efficient methods developed for either axially invariant parallel shear flow [3] or arbitrary three-dimensional flow [4]. The present explicit analytical result is complementary to these, in that general trends are easily detected and quantified, albeit for an axisymmetric plug flow model only.

Finally, it is interesting to note that as part of his wide-ranging contribution to GA calculation methods in mean flow, Candel [4] presented a number of predictions based on ray theory for sources in a jet flow, located both on and off the axis, and his numerical results illustrate several of the features discussed in section 4 of the present paper.

### 1.3. OFF-AXIS SOURCES: OUTLINE OF THE INVESTIGATION

The GA shear layer corrections developed in references [1, 2] are restricted to sources on the axis of the open jet. When an installed-engine model is placed in the jet, however, the sound from an engine exhaust placed on the centreline may be scattered by surfaces relatively far from the jet axis. The question then arises of whether significantly different shear layer corrections are needed for such off-axis sources.

To explore this question, the standard GA correction algorithm for on-axis sources and cylindrical shear layers [1] has been extended so that sources can be placed at arbitrary radial and azimuthal positions within the flight stream jet; the azimuthal reference here is provided by the external microphone location. Section 2 sets out the theoretical basis of the ray calculation, and in section 3 a generalized correction procedure is developed for off-axis sources radiating through the shear layer.

Obtaining an explicit analytical result for the shear-layer correction factor requires a careful discussion of the ray-tube geometry, as presented in Appendix A. Note that in all cases, the general result contained in equation (33) of section 3.2 remains valid. It relates the power spectrum of the pressure measured in the facility to the desired far-field measurement in flight. The algebraic complication that arises in Appendix A is due entirely to the $dA_n/d\Omega_1$ term in equation (33), which is a measure of the ray-tube area outside the flight stream.

In section 4, the shear layer amplitude correction factor is evaluated numerically in the far field ($r_m/a \to \infty$), for a range of source positions across the flight stream jet and for a realistic

range of flight Mach numbers and emission angles. The key results for this purpose are contained in equations (33) and (A44). Confirmation of the analytical ray-tube area result is provided by examining three special cases in Appendices B, C, and D:

- Measurement microphone in the geometric far field: $(r_m/a \to \infty)$.
- Measurement microphone immediately outside the jet: $(r_m/a = 1)$.
- Source on the jet centreline: $(r_s/a \to 0)$.

Here $r_m$ is the measurement radius (distance of the microphone from the jet axis), $r_s$ is the source radius, and $a$ is the radius of the jet (for a complete list of symbols, see Appendix E).

## 2. THEORETICAL ANALYSIS OF REFRACTION CORRECTIONS

The analysis is based on an idealized model of the flow field, in which the flow is parallel and axisymmetric and the jet shear layer remains thin compared with the nozzle diameter. Use of GA means the shear layer correction is source-independent. The following nomenclature is used throughout.

Region 1 = flight simulation jet; modelled as a top-hat profile, velocity $U$ = const.

Region 0 = exterior region, fluid at rest.

The $x$-axis points downstream, and cylindrical co-ordinates $(r, \phi, x)$ are used; the model flow field does not vary with $x$. Figure 1 shows the ray geometry, for a typical ray leaving the source at A and crossing the jet shear layer at B.

### 2.1. DOPPLER RELATION

For a given axial wavenumber $k_x$, frequencies $\omega_0$ relative to the outer fluid (at rest in the laboratory reference frame) and $\omega_1$ relative to the flight simulation flow field (i.e., moving at velocity $U$) are related by

$$\omega_0 = \omega_1 + k_x U. \tag{1}$$

We introduce the polar angles $(\theta_1, \theta_0)$ defined by

$$\cos\theta_1 = k_x c_1/\omega_1 = k_x/k_1 \quad \text{(inside the flow)},$$
$$\cos\theta_0 = k_x c_0/\omega_0 = k_x/k_0 \quad \text{(outer region)}: \tag{2}$$

they represent the angles made by the wavenormal with the jet axis, inside and outside the jet. Substituting $\omega_1 = k_x c_1/\cos\theta_1$ and $\omega_0 = k_x c_0/\cos\theta_0$ into equation (1) gives

$$c_0/\cos\theta_0 = c_1/\cos\theta_1 + U,$$

i.e.,

$$\cos\theta_0 = (c_0/c_1)\, D_1 \cos\theta_1. \tag{3}$$

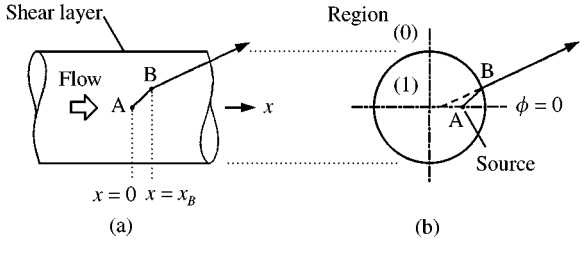


Figure 1. Ray geometry. (a) Side view. (b) View along the $x$-axis.

Equation (3) relates the wavenormal angles inside and outside the flow. The Doppler factor $D_1$, defined below, is the ratio of the frequency heard by an observer moving with the flow inside the jet and the frequency in a fixed frame. These two frequencies are related by

$$\omega_1/\omega_0 = D_1 = (1 - U/c_0 \cos\theta_0) = (1 + U/c_1 \cos\theta_1)^{-1}. \tag{4}$$

### 2.2. TRANSVERSE WAVENUMBERS AND REFRACTION

In the plane normal to the $x$-axis, the wavenumbers in regions (1, 0) are denoted by $K_1$, $K_0$. They are related to $k_x$ by

$$K_1^2 + k_x^2 = (\omega_1/c_1)^2, \qquad K_0^2 + k_x^2 = (\omega_0/c_0)^2. \tag{5}$$

Note that the same axial wavenumber $k_x$ applies inside and outside the jet. The $(K_1, K_0)$ relations above can be rewritten in terms of $\theta_0$ or $\theta_1$, rather than $k_x$, by using equations (2) and (4): thus

$$(K_1 c_0/\omega_0)^2 = (c_0/c_1)^2 D_1^2 - \cos^2\theta_0, \qquad (K_1 c_1/\omega_1)^2 = \sin^2\theta_1, \tag{6}$$

$$(K_0 c_0/\omega_0)^2 = \sin^2\theta_0, \qquad (K_0 c_1/\omega_1)^2 = (c_1/c_0)^2 D_1^{-2} - \cos^2\theta_1. \tag{7}$$

In the transverse plane, the ray emerging at B from the jet has angles of incidence and transmission $(\alpha_1, \alpha_0)$, respectively, defined relative to the local normal at the interface between regions 1 and 0 (see Figure 2).

Conservation of the transverse wavenumber parallel to the interface gives

$$K_1 \sin\alpha_1 = K_0 \sin\alpha_0 \tag{8}$$

which is a form of Snell's law. Note that the ray and wavenormal directions projected onto the transverse plane are the same, since the flow is assumed to be axial.

Combining equations (6)–(8), and writing $(c_0/c_1)\, D_1$ as $E$, gives

$$\left(\frac{\sin\alpha_0}{\sin\alpha_1}\right)^2 = \left(\frac{K_1}{K_0}\right)^2 = \frac{\sin^2\theta_1}{(E^{-2} - \cos^2\theta_1)} = \frac{(E^2 - \cos^2\theta_0)}{\sin^2\theta_0}. \tag{9}$$

Equation (9) allows rays to be traced in the transverse plane from a source at A, via the shear layer at $B$, to points in the exterior field.

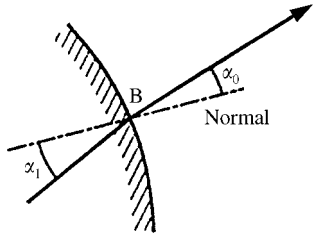


Figure 2. Refraction in transverse plane.

### 2.3. RAY TRACING

A ray starts from the source at A, at $(r_s, 0, 0)$ in cylindrical co-ordinates $(r, \phi, x)$, and crosses the jet shear layer at B. The aim is to find the co-ordinates of B, and the trajectory of the emerging ray, in terms of the ray launch angle $\lambda$ in the transverse plane (see Figure 3).

#### 2.3.1. *Azimuthal location of ray crossing*

In cylindrical co-ordinates, Figure 3 locates the crossing point B at

$$r_B = a \quad (= \text{jet radius}), \qquad \phi_B = \lambda - \alpha_1. \tag{10, 11}$$

The angle of incidence $\alpha_1$ is related to $\lambda$ by

$$r_s/\sin\alpha_1 = a/\sin\lambda,$$

i.e.,

$$\sin\alpha_1 = (r_s/a)\sin\lambda. \tag{12}$$

From equations (11) and (12),

$$\phi_B = \lambda - \sin^{-1}((r_s/a)\sin\lambda). \tag{13}$$

#### 2.3.2. *Axial and transverse ray velocity components*

To find $x_B$ one needs to consider the ray velocity vector $\mathbf{v}$ in the jet. Its axial component is

$$v_x = c_1\, n_{1x} + U, \tag{14}$$

where $\mathbf{n}_1$ is the unit wavenormal vector in the flow. In terms of $k_x$,

$$n_{1x} = k_x/k_1 = k_x c_1/\omega_1 = \cos\theta_0/E = \cos\theta_1, \tag{15}$$

where $E = k_1/k_0 = (c_0/c_1)D_1$ was first introduced in equation (9).

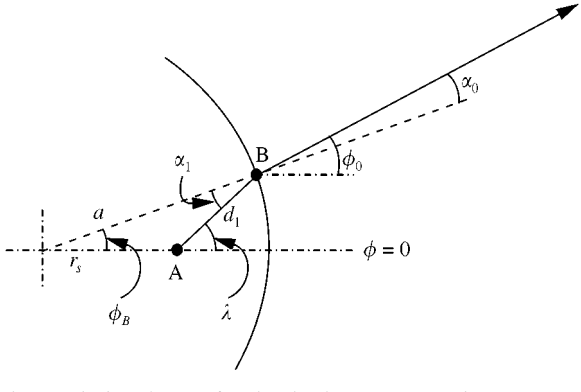


Figure 3. Source emission angle $\lambda$ and ray refraction in the transverse plane. Transverse distance $AB = d_1$.

The component of $\mathbf{v}$ in the transverse plane has magnitude

$$v_t = c_1\, n_{1t}, \tag{16}$$

where $n_{1t}$ is the magnitude of the component of $\mathbf{n}_1$ in the transverse direction. It is related to $n_{1x}$ and the wavenormal angles by

$$n_{1t} = \sqrt{1 - n_{1x}^2} = \sqrt{1 - (\cos\theta_0/E)^2} = \sin\theta_1. \tag{17}$$

2.3.3. *Axial distance travelled by ray in jet flow*

The ratio of $v_x$ to $v_t$ gives the ratio of distances travelled by the ray, in a given time, parallel and perpendicular to the $x$-axis. Thus if $d_1$ is the transverse distance between A and B (Figure 3), given by

$$d_1 = a \sin\phi_B/\sin\lambda, \tag{18}$$

it follows that

$$x_B/d_1 = v_x/v_t = (c_1 n_{1x} + U)/c_1 n_{1t} \tag{19}$$

from equations (14) and (16) above. This expression can be rewritten, using equations (15) and (17), in the alternative forms

$$\frac{x_B}{d_1} = \left(\frac{\cos\theta_0}{E} + \frac{U}{c_1}\right) \Bigg/ \sqrt{1 - \left(\frac{\cos\theta_0}{E}\right)^2} = \frac{(\cos\theta_1 + U/c_1)}{\sin\theta_1}. \tag{20}$$

2.3.4. *Summary of ray-crossing location results*

The cylindrical co-ordinates of the point B where the emerging ray crosses the shear layer, i.e. $(x_B, \phi_B, a)$, are now defined. Choose as independent variables the source radius $r_s$; the ray launch angle, $\lambda$, in the transverse plane; and the wavenormal angle in the flow, $\theta_1$, measured from the jet axis. Then

- $x_B$ is given by equation (18) and (20) above, and
- $\phi_B$ is given by equation (13) above.

## 2.4. RAY GEOMETRY IN OUTER REGION

The emerging ray outside the jet flow has a unit wavenormal vector $\mathbf{n}_0$. The direction of $\mathbf{n}_0$ can be specified in terms of azimuthal and polar angles, $(\phi_0, \theta_0)$, as in Figures 3 and 4. The polar angle $\theta_0$ has already been introduced in equation (2), and $\phi_0$ is the ray orientation in the transverse plane; it corresponds to the azimuthal co-ordinate of a farfield point on the ray. Thus,

$$\begin{aligned} \phi_0 &= \lambda - \alpha_1 + \alpha_0 \quad \text{(see Figure 3)} \\ &= \lambda - \sin^{-1}\left(\frac{r_s}{a}\sin\lambda\right) + \sin^{-1}\left(\frac{K_1}{K_0}\frac{r_s}{a}\sin\lambda\right) \end{aligned} \tag{21}$$

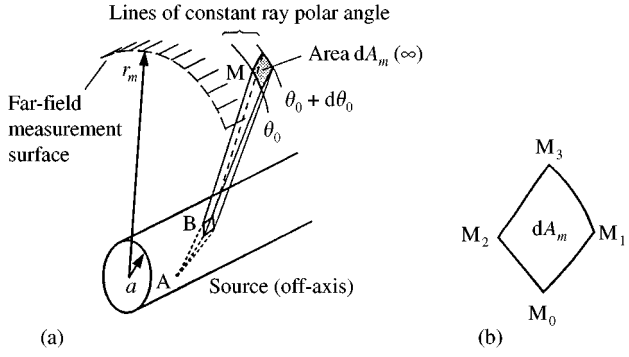


Figure 4. (a) Ray tube geometry between source and far field point. (b) Enlargement of ray tube intersection with the cylindrical surface $r = r_m$, in the far field ($r_m \gg a$).

from equations (8), (12) and (13). The polar angle $\theta_0$ is given by

$$\cos\theta_0 = E\cos\theta_1 \qquad (E = c_0 D_1/c_1). \tag{22}$$

2.4.1. *Ray-tube solid angles*

In order to apply an energy conservation argument to relate the mean-square pressures in regions (0) and (1), we shall need to calculate the ratio $dA_n/d\Omega_1$. Here $dA_n$ is the ray-tube cross-sectional area in region (0) outside the jet (see Figure 4), which in the far field is simply related to the ray-tube solid angle $d\Omega_0$ by

$$d\Omega_0 \approx \frac{dA_m \sin^3\theta_0}{r_m^2} = \frac{dA_n \sin^2\theta_0}{r_m^2} \quad (r_m/a \to \infty). \tag{23}$$

The solid angle $d\Omega_1$ is defined by the corresponding $\mathbf{n}_1$ directions inside the jet flow. Note that $d\Omega_1$ is not the *ray-tube* solid angle inside the jet flow, but the *wavenormal* solid angle. Thus

$$d\Omega_1 = |d\lambda\, d(\cos\theta_1)|. \tag{24}$$

## 3. FACILITY DATA CORRECTION: SUMMARY OF OBJECTIVES

Figure 5 shows the comparison between the ray path ABM in the flight simulation facility and the corresponding ray path ABN in the true flight situation, with the frame of reference in both cases chosen to make the source stationary. The autospectral densities of the acoustic pressure at M in the flight-simulation facility (outside the jet but not necessarily in the geometric far field), and at N in the flight situation (with the microphone in the far field), are respectively $P_m(\omega)$ and $P_\infty(\omega)$. Both are measured in the aircraft reference frame

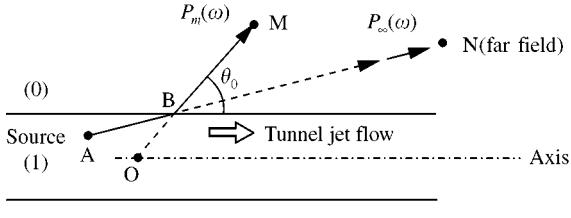


Figure 5. Flight simulation versus the true flight situation: comparison of ray paths.

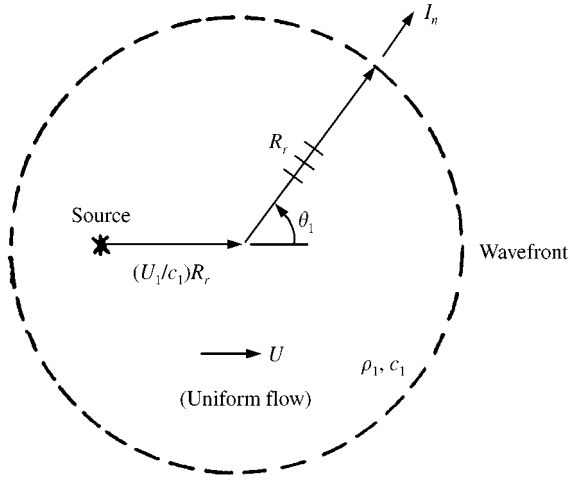


Figure 6. Definition of intensity component normal to wavefront.

(previously distinguished by subscript 0); the 0 subscript on $\omega$ is dropped here for convenience.

"Corresponding ray paths" means that the wavenormal $\mathbf{n}_1$ inside the flow is the same in both cases (1) and (2). Given this correspondence, the ratio $P_m(\omega)/P_\infty(\omega)$ can be predicted within the limitations of geometrical acoustics, without the need for source information. It then follows that measured $P_m(\omega)$ values can be processed to yield $P_\infty(\omega)$. We note the following practical points:

- Data are assumed to be collected at discrete positions outside the open jet. Typical values of $r_m/a$ in current facilities range from 10 to 40.
- The objective is to convert $P_m(\omega)$ measurements into $R_r^2 P_\infty(\omega)$ values, for selected emission angles $(\lambda, \theta_1)$ within the flow. Symbol $R_r$ denotes the distance travelled by an acoustic wavefront relative to the fluid, as indicated in Figure 6.
- This will involve interpolating between measurement points to get the desired $(\lambda, \theta_1)$ combination, and then applying correction factors to the interpolated measured $P_m(\omega)$ values.

### 3.1. RELATION BETWEEN MEASUREMENT POSITION AND SOURCE EMISSION ANGLES

The same cylindrical co-ordinates are used to locate M as were used for A and B (Figures 1–3). Thus the $(r, \phi, x)$ co-ordinates for these points are

(source point A) $r_s, \quad 0, \quad 0,$
(shear layer B) $a, \lambda - \alpha_1, x_B$ [equations (20), (18) give $x_B$],
(microphone M) $r_m, \quad \phi_m, \quad x_m.$

The aim is to relate $(\phi_m, x_m)$ to $(\lambda, \theta_1)$, for given values of $r_m$, $r_s$, and $a$.

#### 3.1.1. *Azimuthal measurement position*

From Figure 7,

$$\phi_m = (\lambda - \alpha_1) + (\alpha_0 - \delta), \tag{25}$$

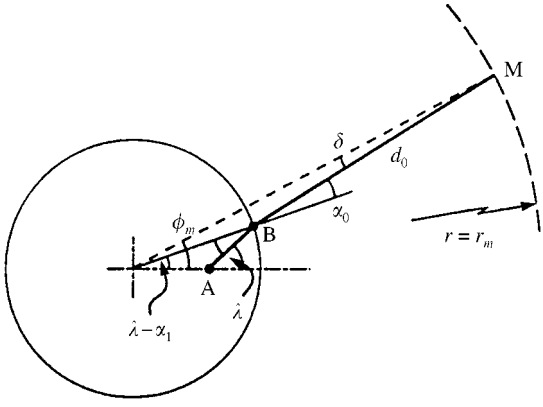


Figure 7. Geometry for calculation of measurement azimuth angle. Transverse distance BM = $d_0$.

where

$$a/\sin\delta = r_m/\sin\alpha_0. \tag{26}$$

It follows that

$$\phi_m = \lambda - \alpha_1 + \alpha_0 - \sin^{-1}((a/r_m)\sin\alpha_0). \tag{27}$$

Note that $\alpha_1$ is related to $\lambda$ by equation (12), and $\alpha_0$ to $\alpha_1$ by equation (9). Therefore $\phi_m(\lambda, \theta_1)$ can be calculated, for any given values of $r_s/a$ and $r_m/a$, using equations (9), (12), and (27).

### 3.1.2. *Axial measurement position*

The axial displacement $(x_m - x_B)$ follows from a calculation similar to that used earlier to find $x_B$ (see sections 2.3.2 and 2.3.3); but since this segment of the ray path lies outside the jet, there is no complication arising from flow convection. Thus

$$\frac{(x_m - x_B)}{d_0} = \frac{n_{0x}}{n_{0t}} = \frac{\cos\theta_0}{\sin\theta_0} = \frac{E\cos\theta_1}{\sqrt{1 - E^2\cos^2\theta_1}}. \tag{28}$$

The distance $d_0$ is the projection of BM on the transverse plane (see Figure 7); using equations (25)–(27) gives

$$\begin{aligned} d_0 &= r_m \frac{\sin(\alpha_0 - \delta)}{\sin\alpha_0} \\ &= r_m \frac{1}{\sin\alpha_0} \sin\left\{\alpha_0 - \sin^{-1}\frac{a}{r_m}\sin\alpha_0\right\}. \end{aligned} \tag{29}$$

As was noted in the previous section, $\alpha_0$ can be found from $(\lambda, \theta_1)$ using equations (9) and (12). Given $\alpha_0$, $(x_m - x_B)/a$ can be calculated from equations (28) and (29), as a function of $(\lambda, \theta_1)$ and the parameters $(r_s/a, r_m/a)$.

## 3.2. AMPLITUDE CORRECTION

The analysis of section 3.1 allows the ray position $(\phi_m, x_m)$ to be identified, on the near-field cylindrical surface $r = r_m$, for any combination of source emission angles $(\lambda, \theta_1)$ in

the jet flow. The next step is to convert the measured $P_m(\omega)$ value to an equivalent $R_r^2\, P_\infty(\omega)$ value in the true flight situation.

The approach adopted is that used in reference [1]. Based on the GA approximation, the acoustic energy flow along a ray tube—such as that in Figure 4—is conserved. If $\mathrm{d}W_1(\omega)$ denotes the power travelling along section AB of the ray tube, per unit angular frequency in a reference frame attached to the facility (or aircraft), and $\mathrm{d}W_0(\omega)$ is the power in the same ray tube after it emerges from the jet, then energy conservation means that

$$\mathrm{d}W_1(\omega) = \mathrm{d}W_0(\omega). \tag{30}$$

(a) Outside the flow, $\mathrm{d}W_0(\omega)$ is related to the measured power spectrum of acoustic pressure $P_m(\omega)$ as follows:

$$\mathrm{d}W_0(\omega) = \mathrm{d}A_n/\rho_0\, c_0\, P_m(\omega). \tag{31}$$

Here $\mathrm{d}A_n$ is the ray-tube cross-sectional area (measured normal to the ray direction), at the measurement location $M$ outside the jet (see Figures 5 and 7). It is not the same as $\mathrm{d}A_m$ (measured on the cylindrical surface $r = r_m$; see Figure 4).

(b) Inside the flow, $\mathrm{d}W_1(\omega)$ is related to the farfield quantity $R_{r\infty}^2\, P_\infty(\omega)$ that would ideally be measured in the true flight situation. The relationship is

$$\mathrm{d}W_1(\omega) = \frac{\mathrm{d}\Omega_1}{\rho_1 c_1 D_1^2} R_{r\infty}^2\, P_\infty(\omega) \tag{32}$$

and follows from equation (15) of reference [1].

Equating expressions (31) and (32) gives

$$R_{r\infty}^2\, P_\infty(\omega) = \frac{\rho_1 c_1 D_1^2}{\rho_0 c_0} \frac{\mathrm{d}A_n}{\mathrm{d}\Omega_1} P_m(\omega). \tag{33}$$

This is a key result, as it provides a conversion from the near field measurement $P_m(\omega)$ made in the facility outside the shear layer, to the desired farfield measurement that would be made in the true flight situation without the shear layer. The frame of reference in both cases is attached to the source (aircraft).

### 3.2.1. *Calculation of* $\mathrm{d}A_n/\mathrm{d}\Omega_1$ *factor*

The solid angle $\mathrm{d}\Omega_1$ is related to the incremental source emission angles, $\mathrm{d}\lambda$ and $\mathrm{d}\theta_1$, by equation (24). However, the cross-sectional area $\mathrm{d}A_n$ of the emerging ray tube in the geometric near field is a complicated function of several variables:

$$\mathrm{d}A_n = a^2\, \mathrm{d}\lambda\, \mathrm{d}\theta_1\, f(\lambda, \theta_1, U_1/c_1, c_0/c_1, r_s/a, r_m/a). \tag{34}$$

There are two special cases where $\mathrm{d}A_n/\mathrm{d}\Omega_1$ is relatively straightforward to calculate, and which can be used to test the general analysis of Appendix A: they are (1) measurement position immediately outside the shear layer, i.e., at point B in Figures 1–6; and (2) source position on the jet centreline.

The exact calculations for these two cases are presented in Appendices B and C. Meanwhile in section 3.2.2 below an approximation is presented which is asymptotically valid in the farfield, and which is relatively simple to derive; the general exact result, which can be obtained analytically but is considerably more complicated, is developed in Appendix A.

3.2.2. *Approximation to* $dA_n/d\Omega_1$ *factor*

For distances $r_m$ from the jet axis which are not too small (say $r_m/a > 10$), it may be sufficiently accurate to estimate $dA_n$ from the farfield expression

$$dA_n \approx R_{r0}^2 \, d\Omega_0. \tag{35}$$

Here $d\Omega_0$ is the ray-tube solid angle in the outer region [region (0)]. Further information on ray geometry in this region, in the farfield limit, is provided in Figure 4 and section 2.4. The distance $R_{r0}$ is shown as OM in Figure 5; it is based on projecting the farfield refracted ray back to the jet axis, and is given by

$$R_{r0} = r_m/\sin\theta_0. \tag{36}$$

Equations (23), (35) and (36) give the approximate relation

$$dA_n/r_m^2 \approx \sin\theta_0 \, (dA_m/r_m^2)_{r_m \to \infty}. \tag{37}$$

The $\sin\theta_0$ factor in this result is expected, since $dA_m$ has its normal at angle $\theta_0$ to the ray direction.

The last factor on the right of equation (37) is evaluated in Appendix D. Combining equation (D9) from Appendix D with equation (37) above gives

$$dA_n/r_m^2 \approx (1 - \beta_1 + \beta_0) \frac{c_1}{c_0} \frac{E^2 \sin\theta_1}{(1 - E^2 \cos^2\theta_1)} \, d\lambda \, d\theta_1. \tag{38}$$

As a check on this result, note that for on-axis sources (i.e., $\beta_1 = \beta_0 = 0$) it reproduces the exact farfield expression

$$(dA_n/R_{r0}^2)_{\text{farfield}} = d\Omega_0 = d\lambda \sin\theta_0 \, d\theta_0. \tag{39}$$

The equivalence of equations (38) and (39) in this situation can be demonstrated by first using equation (36) to replace $R_{r0}$, and then using equation (3) above with equation (D6) from Appendix D to replace $\theta_0$ by $\theta_1$.

Finally, when equations (24) and (38) are used to substitute for $d\Omega_1$ and $dA_n$ in equation (33), one obtains the following *approximate* equation for correcting measured power spectra to their equivalent farfield flight values:

$$R_{r\infty}^2 P_\infty(\omega) = \frac{\rho_1}{\rho_0} D_1^4 \frac{r_m^2 P_m(\omega)}{1 - ((c_0/c_1) D_1 \cos\theta_1)^2} (1 - \beta_1 + \beta_0). \tag{40}$$

As mentioned above, the exact version of equation (40) is given in Appendix A. An interpretation of the various factors in equation (40) is presented in the following sections.

## 3.3. INTERPRETATION OF THE FLIGHT-FACILITY AMPLITUDE CORRECTION EQUATION

- Equation (40), or its generalized version equation (33), converts power spectra of sound pressure measured outside the jet, on a cylinder of radius $r_m$ concentric with the jet axis, to equivalent farfield flight values.
- The measurement location on the cylinder $r = r_m$ is chosen to correspond with the desired source emission angles $(\lambda, \theta_1)$. For this purpose, microphone co-ordinates $(\phi_m, x_m)$ are chosen as described in section 3.1.

- The polar emission angle $\theta_1$ is the wavenormal polar angle within the jet flow, referred to a polar axis pointing in the flight stream direction. It also corresponds to the flyover polar angle based on the aircraft position at the emission time.
- The farfield distance $R_r$ is the distance travelled by the wavefronts in the true flight situation. In aircraft co-ordinates, the atmosphere is moving and $R_r$ is the distance travelled relative to the fluid. Note that for an aircraft flying past a fixed observer in a still atmosphere, $R_r$ is the source–observer distance in the far field, measured at the emission time.
- The final factor on the right of equation (40) accounts for off-axis source locations. It is an approximation, valid when $r_m/a$ is greater than 3 or so, which can be checked against the exact special-case results presented below.
- The next-to-last factor in equation (40) represents $R_{r0}^2 P_m(\omega)$.
- The factor $(\rho_1/\rho_0)D_1^4$ is what was called the "facility correction factor" in reference [1]. It represents the amplitude correction factor, for on-axis sources and a farfield observer, required to correct for refraction through the shear layer after scaling for distance by $(R_{r0}/R_{r\infty})^2$.
- All frequencies in equation (40), or its generalized version equation (33), are measured relative to the source (aircraft). Using a ground-based microphone is equivalent to measuring the frequency relative to the flow, and yields Doppler shifted frequencies $D_1\omega = \omega_1$. Thus if $P_g(\omega_1)$ is the power spectrum measured by a ground-based observer at the same emission distance $R_{r\infty}$, the two power spectra are related by

$$\omega_1 \, P_g(\omega_1) = \omega P_\infty(\omega). \tag{41}$$

  Equation (41) implies that proportional-bandwidth levels (measured in 1/3-octave bands, for example) are the same for both observers.
- One may wish to convert proportional-band facility measurements at frequency $\omega$ into equivalent farfield flyover data at $\omega_1$, as measured by a stationary observer on the ground. It follows from equations (33) and (41) that

$$R_{r\infty}^2 \omega_1 P_g(\omega_1) = \frac{\rho_1 c_1 D_1^2}{\rho_0 c_0} \frac{\mathrm{d}A_n}{\mathrm{d}\Omega_1} \omega P_m(\omega). \tag{42}$$

  The angular frequencies which appear in equation (42) may conveniently be replaced by ordinary frequencies in Hz.

## 4. NUMERICAL STUDY OF OFF-AXIS EFFECTS

### 4.1. FACILITY TRANSMISSION COEFFICIENT

Here we consider the correction required in the pressure spectrum level as measured in the flight simulation facility, in order to arrive at the true spectrum level as measured in the far field when an aircraft flies overhead. This is conveniently quantified by introducing the *facility transmission coefficient*, which is the quantity $T$ defined in equation (43) below:

$$\frac{(r_m^2 + x_m^2)P_m(\omega)}{R_{r\infty}^2 P_\infty(\omega)} = \frac{\rho_0 c_0}{\rho_1 c_1} T. \tag{43}$$

The quantity $T$ depends on the geometry, the Mach number $M$, and the sound speed ratio $c_1/c_0$ (set equal to 1 in the numerical results). Note that the numerator and the denominator on the left of equation (43) relate to the same ray. According to equation (33), $T$ is given for

an off-axis source by

$$T = D_1^2(r_m^2 + x_m^2)\,|\mathrm{d}A_n/\mathrm{d}\Omega_1|^{-1}. \tag{45}$$

A convenient reference value for $T$ is that which applies to an on-axis source and a measurement point far from the jet ($r_m/a \to \infty$); it is given by

$$T_0 = (c_1/c_0)D_1^4 \text{ [compare equation (20), reference [1]]}. \tag{46}$$

The same result may also be obtained from equation (A50) of the present paper.

For a source polar emission angle in the forward arc ($\theta_1 = 120°$), Figure 8 shows contours of the logarithmic ratio

$$\Delta L_T = 10\log_{10}(T/T_0), \tag{47}$$

plotted in as a function of $\lambda$ and the source position $r_s/a$; a farfield measurement point is assumed. Note that at an azimuthal angle $\lambda = 90°$, $T$ equals its on-axis value. The deviation $\Delta L_T$ increases in magnitude with $r_s/a$, but is of opposite sign on either side of $\lambda = 90°$. The other feature of Figure 8 is the "rim" in the upper part of the figure; here $\Delta L_T \to \pm\infty$. This is the boundary of total internal reflection from the shear layer; it has the form

$$(r_s/a)\sin\lambda = \text{const.} \tag{48}$$

A similar plot is shown in Figure 9, but for an angle in the rear arc ($\theta_1 = 60°$) rather than the forward arc. There is no total internal reflection and no "rim" appears. The other difference is that the signs of $\Delta L_T$ on either side of $\lambda = 90°$ are reversed.

## 4.2. TOTAL INTERNAL REFLECTION

We continue to take $c_1/c_0$ equal to 1 in this section, in order to explore the regions of total internal reflection and multipath arrival predicted by ray acoustics. As the polar angle $\theta_1$ is

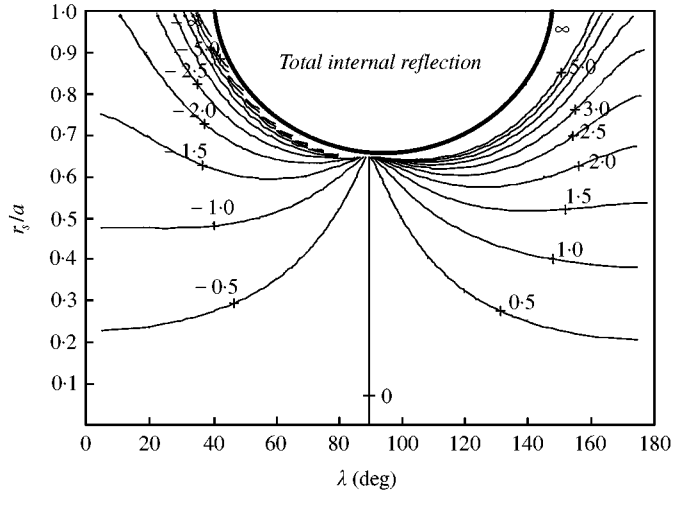


Figure 8. Transmission coefficient ratio in decibels, $\Delta L_T = 10\log_{10}(T/T_0)$, for sound emitted at a polar angle $\theta_1 = 120°$ in the far field (forward arc); jet Mach number $M = 0{\cdot}5$. Coordinates are azimuthal launch angle $\lambda$ and source position $r_s/a$.

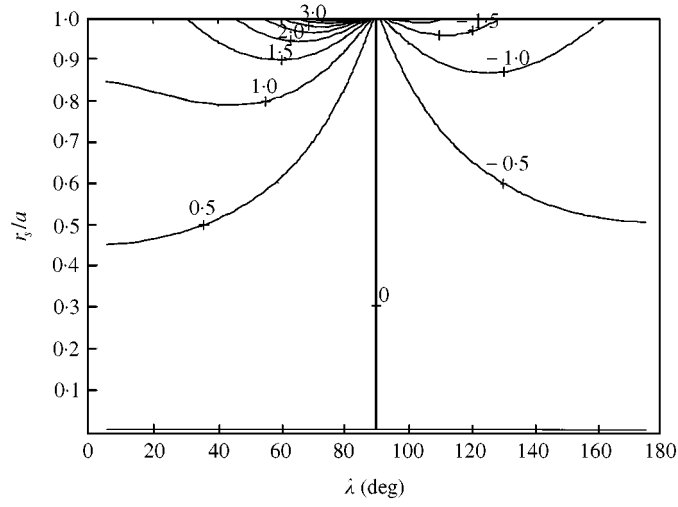


Figure 9. Transmission loss ratio $10 \log_{10}(T/T_0)$ for a source polar emission angle in the rear arc of $\theta_1 = 60°$, an observer in the far field and $M = 0{\cdot}5$, plotted as a function of $\lambda$ and source position $r_s/a$.

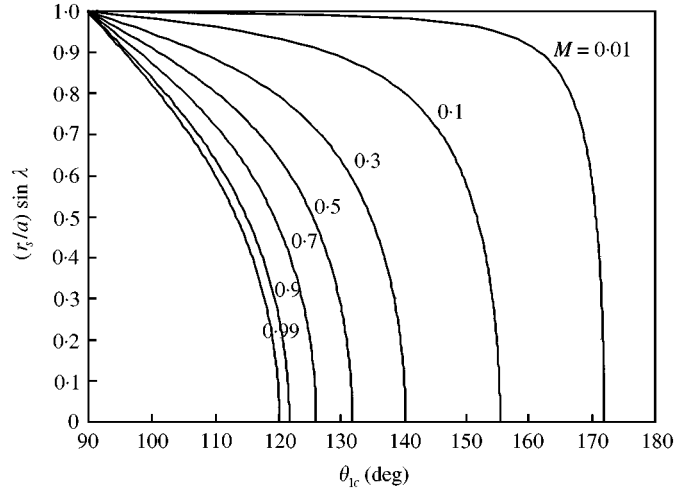


Figure 10. Relationship between $\theta_{1c}$, source position $r_s/a$ and jet Mach number $M$.

increased, total internal reflection (denoted by $\theta_1 = \theta_{1c}$) first occurs for $\lambda = 90°$, and the process is complete once the rays emitted at $\lambda = 0°$ or $180°$ are totally reflected. The corresponding lower and upper critical polar angles, $\theta_{1c}\,(\lambda = 90°)$ and $\theta_{1c}\,(\lambda = 0°)$, are called $\theta_{1l}$ and $\theta_{1u}$. Figure 10 shows the dependence of the total internal reflection angle $\theta_{1c}$ on $(r_s/a)\sin\lambda$ and the jet Mach number, for $C = 1$; the equation connecting these quantities is

$$r_s/a \sin\lambda = \sqrt{\frac{C^2(1 + M\xi_c)^2 - \xi_c^2}{(1 - \xi_c^2)}} \quad (C = c_1/c_0,\ \xi_c = \cos\theta_{1c}). \tag{49}$$

Figure 11 shows explicitly how $\theta_{1c}$ varies with $\lambda$, for various source positions and a Mach number of 0·5. The symmetry either side of $\lambda = 90°$ is apparent, and also the fact that $\theta_{1u}$ is independent of $r_s/a$; both these features are readily predictable from equation (49).

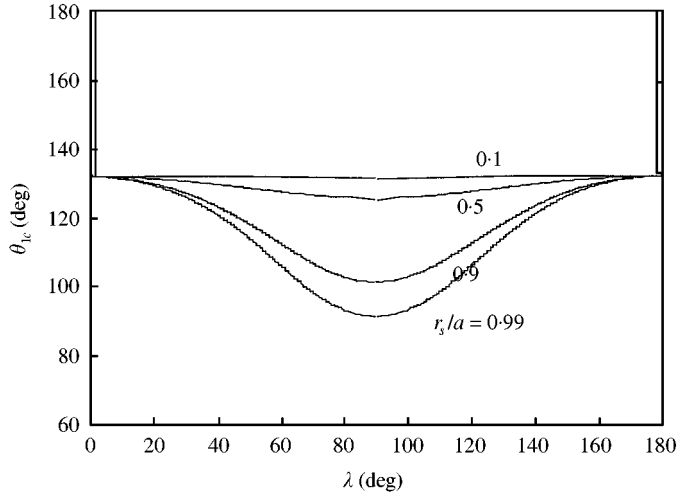


Figure 11. Variation of $\theta_{1c}$ with $\lambda$ for various source positions at a Mach number of 0·5.

### 4.3. AMBIGUITY OF LAUNCH ANGLE IN THE TRANSVERSE PLANE

For an observer outside the jet in the forward arc (strictly, for $\theta_1 > \theta_{1l}$) there is a possibility that two distinct rays from the same off-axis source will emerge from the jet travelling in the same direction. In mathematical terms, the relationship between launch angle $\lambda$ and farfield azimuthal angle $\phi_0$ for given $\theta_1$ becomes multivalued over part of the $(\lambda, \phi_0)$ plane. This phenomenon was noted by Goldstein [3]; it implies that an observer will be unable to distinguish the two contributions without some additional information about the source.

Figure 12 shows the region of ambiguity as the dark-shaded area in the $(\lambda, \theta_1)$ plane, for a jet Mach number of 0·5 and an off-axis source position of $r_s/a = 0·9$; a farfield observer is again assumed ($r_m/a \to \infty$). The adjacent light-shaded areas correspond to unambiguous transmission of a single ray to the observation point, and the unshaded area (to the right of the $\theta_1 = \theta_{1c}$ boundary) corresponds to total internal reflection.

It is convenient to define three regions along the $\theta_1$-axis, marked I–III in Figure 12. Region I, defined by $\theta_1 < \theta_{1l}$, has unambiguous transmission through the jet for all $\lambda$; note that $\theta_{1l}$ is obtained from equation (49) as $\theta_{1c}$ ($\lambda = 90°$). Region II, defined by $\theta_{1l} < \theta_1 < \theta_{1u}$, has unambiguous transmission over only part of the $\lambda$ range: clearly, as soon as $\theta_1$ exceeds $\theta_{1l}$, ambiguous behaviour is seen over some part of the transmitted range of launch angles $\lambda$, and measurements outside the shear layer can no longer be meaningfully interpreted. The upper limit of region II is obtained from equation (49) as $\theta_{1c}$ ($\lambda = 0°$). Finally, region III allows no transmission at all outside the jet, according to ray acoustics.

## 5. SUMMARY AND CONCLUSIONS

1. A simplified model of the open-jet type of flight simulation facility has been used to study the refraction corrections needed for sources located off the flight-stream axis. The mean flow model consists of a uniform parallel jet, separated from the outer stationary fluid by a thin shear layer (thickness $\delta \ll$ jet radius). The density and sound speed in the jet are allowed to be different from those in the ambient fluid.

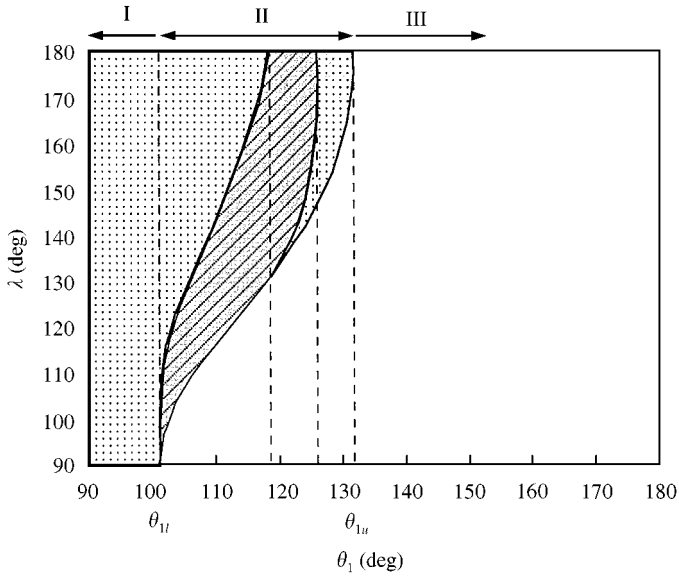


Figure 12. Region of ambiguity (dark area) in the $(\lambda, \theta_1)$ plane, for a far field obsever. The region of inambiguous transmission is represented by light shading, and the region of zero transmission (total internal reflection) is unshaded. Jet Mach number $M = 0{\cdot}5$; off-axis source position $r_s/a = 0{\cdot}9$; $c = 1$.

2. In the radiation model a point source of arbitrary directivity is located at an off-axis position within the jet, and its radiation to any position in the outer fluid (i.e., including the geometric near field) is calculated via the geometrical acoustics approximation (GA). The GA approximation strictly requires $\delta/\lambda_{ac}$ to be large, but numerical studies for a plane shear layer in reference [2] have shown the error to be typically less than 0·25 dB even in extreme cases ($\delta/\lambda_{ac} \to 0$, $M = 0{\cdot}5$). The main exception occurs for sound emitted in the forward arc, close to the critical angle.
3. The GA calculation uses ray tracing to identify what microphone positions outside the jet correspond to specified source emission angles inside the flow. Exact analytical expressions are presented for this purpose in section 3.1.
4. Amplitude corrections are then applied along each ray path, to convert facility measurements taken at a finite distance from the jet axis to equivalent farfield flight conditions. The generalized correction procedure is summarized in equation (33) and section 3.3. The advantages of the explicit results presented here, relative to the use of numerical ray tracing as described in references [3, 4], are the insight available from analytical expressions and the relative ease of coding for numerical evaluation.
5. In order to assess the influence of off-axis source location on the shear-layer amplitude correction, a numerical study has been carried out and results are shown in section 4. The influence of source location is generally modest (less than 0·5 dB) for Mach numbers below 0·5 and for source radial locations, $r_s/a$, up to 0·5, but increases rapidly close to the critical angle for total internal reflection.
6. The phenomena of total internal reflection and launch angle ambiguity (due to two different rays reaching the same observation point) make it impossible to interpret measurements beyond a certain angle to the downstream jet axis. This critical polar angle $\theta_{1l}$ is strongly dependent on source radial position, and is determined by equation (49) of section 4.

## ACKNOWLEDGMENTS

The authors are grateful to an anonymous referee for helpful comments. The first author thanks Dr M. J. Fisher for valuable background information, and Dr M. E. Goldstein for discussions relating to his geometrical acoustics theory of sound radiation from sources in a jet flow. Financial support was provided by the U.K. Department of Trade and Industry through the CARAD Programme, and thanks are due to Richard Pinker for his encouragement and interest.

## REFERENCES

1. C. L. MORFEY and B. J. TESTER 1977 *Journal of Sound and Vibration* **54**, 83–106. Noise measurements in a free jet flight simulation facility: shear layer refraction and facility-to-flight corrections.
2. R. K. AMIET 1978 *Journal of Sound and Vibration* **58**, 467–482. Refraction of sound by a shear layer.
3. M. E. GOLDSTEIN 1982 *Journal of Sound and Vibration* **80**, 499–522. High frequency sound emission from moving point multipole sources embedded in arbitrary transversely sheared mean flows.
4. S. M. CANDEL 1977 *Journal of Fluid Mechanics* **83**, 465–493. Numerical solution of conservation equations arising in linear wave theory: application to aeroacoustics.

## APPENDIX A: RAY-TUBE AREA CALCULATION IN THE GENERAL CASE

1. The ray tube shown in Figure A1 is defined by the following four emission directions from the source at A:

$$\begin{aligned} &\text{Ray 0 (the reference ray)} && \theta_1, && \lambda; \\ &\text{Ray 1} && \theta_1 + \mathrm{d}\theta_1, && \lambda; \\ &\text{Ray 2} && \theta_1, && \lambda + \mathrm{d}\lambda; \\ &\text{Ray 3} && \theta_1 + \mathrm{d}\theta_1, && \lambda + \mathrm{d}\lambda. \end{aligned} \tag{A1}$$

   The intersection of the ray tube with the cylinder $r = a$ defines a parallelogram $\mathrm{B_0\,B_1\,B_2\,B_3}$.
2. Figure A2 shows a cross-section of the emerging ray tube in the vicinity of B just outside the jet, normal to the unit vector $\mathbf{n}_0$ (the emerging ray direction). The cross-section $\mathrm{C_0C_1C_2C_3}$ is the projection of $\mathrm{B_0B_1B_2B_3}$ onto the plane normal to $\mathbf{n}_0$. The aim in this appendix is to calculate the cross-sectional area $A(s)$ of the spreading ray tube, as a function of distance $s$ measured along the ray from B. Note that $A(0)$ is equal to $fh$, where $f$ is measured in the $\mathbf{i}_1$ direction and $h$ in the $\mathbf{i}_2$ direction; see Figure A2. The unit vector $\mathbf{i}_1$ is defined to be perpendicular to $\mathbf{n}_0$ and coplanar with $(\mathbf{n}_0, \mathbf{i}_x)$, where $\mathbf{i}_x$ is the unit vector in the $x$ direction. The unit vectors $(\mathbf{i}_1, \mathbf{i}_2, \mathbf{n}_0)$ form a right-handed orthogonal set. They are further illustrated in Figures A3 and A4.
3. The dimensions $f, g, h$ of the parallelogram $\mathrm{C_0C_1C_2C_3}$ in Figure A2 are related to the corresponding dimensions $f', g', h'$ of the parallelogram $\mathrm{B_0B_1B_2B_3}$ by

$$f = f' \sin\theta_0, \qquad g = g' \sin\theta_0, \qquad h = h' \cos\alpha_0. \tag{A2}$$

4. The ray direction outside the jet is given by $(\theta_0, \phi_0)$. These angles are determined by the angles $(\theta_1, \lambda)$ at which the ray is emitted inside the jet. Note that $\phi_0$ is not the *co-ordinate* of a point on the ray, but the ray *orientation* relative to $\phi = 0$. The required relations are

$$\cos\theta_0 = G\left(\xi, \frac{U}{c_1}, \frac{c_1}{c_0}\right) \qquad (\xi = \cos\theta_1), \tag{A3}$$

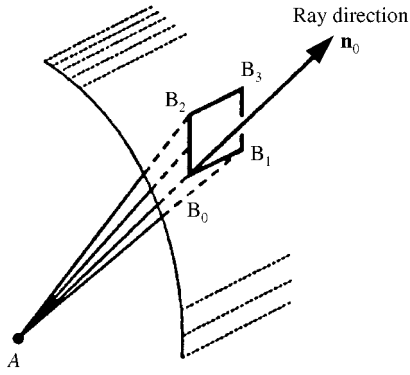


Figure A1. Intersection of ray tube with the edge of the jet ($r = a$). Also shown in the emerging reference ray with direction $\mathbf{n}_0$.

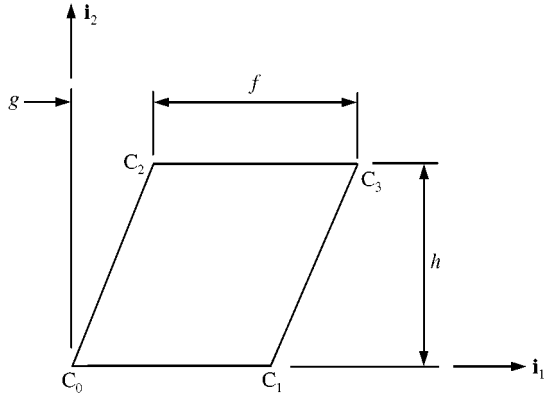


Figure A2. Cross-section of ray tube immediately outside the jet, viewed looking back along the reference ray towards $B_0$; the unit vector $\mathbf{n}_0$ points out of the page. The three unit vectors $\mathbf{i}_1, \mathbf{i}_2, \mathbf{n}_0$ form a right-handed orthogonal set, and remain constant along the ray from $B_0$ to M.

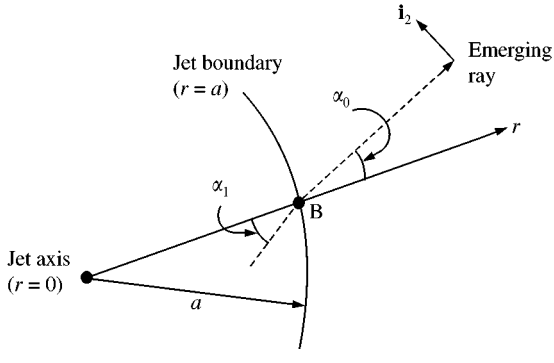


Figure A3. View in $\mathbf{i}_x$ direction (parallel to jet axis), showing the incident and transmitted ray angles at B and the unit vector $\mathbf{i}_2$ normal to the emerging ray in the transverse plane.

$$\phi_0 = \lambda - \sin^{-1}\left((r_s/a)\sin\lambda\right) + \alpha_0. \tag{A4}$$

For details, see equations (21), (22), (6), (7) and (4) of section 2.

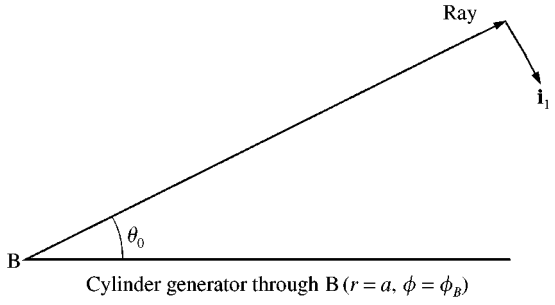


Figure A4. View in $\mathbf{i}_2$ direction, showing the emerging ray (as in Figure A3) and the unit vector $\mathbf{i}$, perpendicular to the ray.

5. It is convenient to locate points ($B_0$, $B_1$, $B_2$, $B_3$) on $r = a$ by means of their cylindrical co-ordinates ($x_B$, $\phi_B$). From equation (13) of section 2, one obtains

$$\phi_B = H(\lambda, r_s/a); \tag{A5}$$

also

$$x_B/a = X(\xi, \lambda, U/c_1, r_s/a) \tag{A6}$$

as follows from section 2, equations (20) and (18).

6. The emerging ray direction $\mathbf{n}_0(\xi, \lambda)$ is conveniently specified in cylindrical components, based on the $(\phi, r)$ co-ordinate directions at point B:

$$(\mathbf{n}_0)_x = \cos\theta_0, \qquad (\mathbf{n}_0)_\phi = \sin\theta_0 \sin\alpha_0, \qquad (\mathbf{n}_0)_r = \sin\theta_0 \cos\alpha_0. \tag{A7}$$

Here angle $\alpha_0$ is defined in Figures 3 and A3. The set of unit vectors $(\mathbf{i}_x, \mathbf{i}_\phi, \mathbf{i}_r)$ is defined to correspond with the local co-ordinate directions $(x, \phi, r)$.

7. In what follows, it will be necessary to convert between local $(x, \phi, r)$ components, based on the $(\mathbf{i}_x, \mathbf{i}_\phi, \mathbf{i}_r)$ unit vectors defined above, and components based on the alternative $(\mathbf{i}_1, \mathbf{i}_2, \mathbf{n}_0)$ system. We therefore begin by expressing $\mathbf{i}_1$ and $\mathbf{i}_2$ in terms of the former system. The unit vector $\mathbf{i}_2$ is given by $(\mathbf{n}_0 \wedge \mathbf{i}_x)/|\mathbf{n}_0 \wedge \mathbf{i}_x|$, where

$$\begin{aligned}(\mathbf{n}_0 \wedge \mathbf{i}_x) &= (\mathbf{i}_x \cos\theta_0 + \mathbf{i}_\phi \sin\theta_0 \sin\alpha_0 + \mathbf{i}_r \sin\theta_0 \cos\alpha_0) \wedge \mathbf{i}_x \\ &= \mathbf{i}_\phi \sin\theta_0 \cos\alpha_0 - \mathbf{i}_r \sin\theta_0 \sin\alpha_0.\end{aligned} \tag{A8}$$

It follows that

$$|\mathbf{n}_0 \wedge \mathbf{i}_x| = \sin\theta_0. \tag{A9}$$

Thus

$$\mathbf{i}_2 = \mathbf{i}_\phi \cos\alpha_0 - \mathbf{i}_r \sin\alpha_0. \tag{A10}$$

8. The unit vector $\mathbf{i}_1$ is given by

$$\mathbf{i}_1 = \mathbf{i}_2 \wedge \mathbf{n}_0. \tag{A11}$$

Thus equations (A7), (A10), and (A11) give

$$\begin{aligned}\mathbf{i}_1 &= (\mathbf{i}_\phi \cos\alpha_0 - \mathbf{i}_r \sin\alpha_0) \wedge (\mathbf{i}_x \cos\theta_0 + \mathbf{i}_\phi \sin\theta_0 \sin\alpha_0 + \mathbf{i}_r \sin\theta_0 \cos\alpha_0)\\ &= \mathbf{i}_x (\sin\theta_0 \cos^2\alpha_0 + \sin\theta_0 \sin^2\alpha_0) + \mathbf{i}_\phi(-\cos\theta_0 \sin\alpha_0) + \mathbf{i}_r(-\cos\theta_0 \cos\alpha_0)\\ &= \mathbf{i}_x \sin\theta_0 - \mathbf{i}_\phi \cos\theta_0 \sin\alpha_0 - \mathbf{i}_r \cos\theta_0 \cos\alpha_0. \qquad \text{(A12)}\end{aligned}$$

It is easy to verify that $\mathbf{i}_1 \cdot \mathbf{i}_2 = 0$, as expected.

9. Calculating the ray-tube area outside the jet (beyond point B) requires a knowledge of the separate directions of the four neighbouring rays. We therefore define the unit-vector increments $(\boldsymbol{\varepsilon}, \boldsymbol{\varepsilon}')$ as follows:

$$\mathbf{n}_0 \text{ (ray 1)} - \mathbf{n}_0 \text{ (ray 0)} = \boldsymbol{\varepsilon}, \qquad \mathbf{n}_0 \text{ (ray 2)} - \mathbf{n}_0 \text{ (ray 0)} = \boldsymbol{\varepsilon}'. \qquad \text{(A13)}$$

These increments are special cases of the general relation

$$\begin{aligned}\mathrm{d}\mathbf{n}_0 &= \mathrm{d}\{\mathbf{i}_x \cos\theta_0 + \mathbf{i}_\phi \sin\theta_0 \sin\alpha_0 + \mathbf{i}_r \sin\theta_0 \cos\alpha_0)\}\\ &= \mathbf{i}_x \mathrm{d}(\cos\theta_0) + \mathbf{i}_\phi[\mathrm{d}(\sin\theta_0 \sin\alpha_0) + \sin\theta_0 \cos\alpha_0\, \mathrm{d}\phi_B]\\ &\quad + \mathbf{i}_r[\mathrm{d}(\sin\theta_0 \cos\alpha_0) - \sin\theta_0 \sin\alpha_0\, \mathrm{d}\phi_B]. \qquad \text{(A14)}\end{aligned}$$

The last step above involves the relations

$$\mathrm{d}\mathbf{i}_x = 0, \qquad \mathrm{d}\mathbf{i}_\phi = (-\mathrm{d}\phi_B)\mathbf{i}_r, \qquad \mathrm{d}\mathbf{i}_r = (\mathrm{d}\phi_B)\mathbf{i}_\phi \qquad \text{(A15)}$$

for the basis vector increments due to a shift in the ray-crossing point B: the four rays cross $r = a$ at four different positions $(\mathrm{B}_0, \mathrm{B}_1, \mathrm{B}_2, \mathrm{B}_3)$, and the differences in $\phi_B$ produce differences in $\mathbf{i}_\phi$ and $\mathbf{i}_r$.

10. From equation (A3) above, with $\cos\theta_1$ written as $\xi$,

$$\mathrm{d}(\cos\theta_0) = (\partial G/\partial\xi)\,\mathrm{d}\xi, \qquad \mathrm{d}(\sin\theta_0) = -\cot\theta_0\, \mathrm{d}(\cos\theta_0). \qquad \text{(A16)}$$

Also, to evaluate equation (A14) we need an expression for $\mathrm{d}\alpha_0$. Equation (21) of section 2 gives

$$\sin\alpha_0 = (K_1/K_0)\,(r_s/a)\sin\lambda = Q(\lambda, \xi, U/c_1, c_1/c_0, r_s/a). \qquad \text{(A17)}$$

Therefore

$$\mathrm{d}(\sin\alpha_0) = (\partial Q/\partial\xi)\,\mathrm{d}\xi + (\partial Q/\partial\lambda)\,\mathrm{d}\lambda, \qquad \mathrm{d}(\cos\alpha_0) = -\tan\alpha_0\, \mathrm{d}(\sin\alpha_0). \qquad \text{(A18)}$$

11. The next step is to express $\mathrm{d}\mathbf{n}_0$ and hence $(\boldsymbol{\varepsilon}, \boldsymbol{\varepsilon}')$ in terms of $(\mathrm{d}\xi, \mathrm{d}\lambda)$, using equations (A5) and (A14)–(A18) above:

$$\begin{aligned}\mathrm{d}\mathbf{n}_0(\mathrm{d}\xi, \mathrm{d}\lambda) &= \mathbf{i}_x G_\xi \mathrm{d}\xi\\ &\quad + \mathbf{i}_\phi[\sin\theta_0(Q_\xi \mathrm{d}\xi + Q_\lambda \mathrm{d}\lambda) + \sin\theta_0 \cos\alpha_0 H_\lambda \mathrm{d}\lambda - \sin\alpha_0 \cot\theta_0 G_\xi \mathrm{d}\xi]\\ &\quad + \mathbf{i}_r[-\sin\theta_0 \tan\alpha_0(Q_\xi \mathrm{d}\xi + Q_\lambda \mathrm{d}\lambda) - \sin\theta_0 \sin\alpha_0 H_\lambda \mathrm{d}\lambda\\ &\qquad\qquad - \cos\alpha_0 \cot\theta_0 G_\xi \mathrm{d}\xi]; \qquad \text{(A19)}\end{aligned}$$

$$\boldsymbol{\varepsilon} = \mathrm{d}\mathbf{n}_0(\mathrm{d}\xi, 0), \qquad \boldsymbol{\varepsilon}' = \mathrm{d}\mathbf{n}_0(0, \mathrm{d}\lambda). \qquad \text{(A20)}$$

12. To calculate $A(s)$, we shall need the components of $\boldsymbol{\varepsilon}$, $\boldsymbol{\varepsilon}'$ in the $\mathbf{i}_1$ and $\mathbf{i}_2$ directions. The scalar products of $\mathrm{d}\mathbf{n}_0$ with $(\mathbf{n}_0, \mathbf{i}_1, \mathbf{i}_2)$ are

$$\begin{aligned}\mathbf{n}_0 \cdot \mathrm{d}\mathbf{n}_0 = &\{G_\xi \cos\theta_0 + [Q_\xi \sin\theta_0 - G_\xi \sin\alpha_0 \cot\theta_0] \sin\theta_0 \sin\alpha_0 \\ &+ [-Q_\xi \tan\alpha_0 \sin\theta_0 - G_\xi \cos\alpha_0 \cot\theta_0] \sin\theta_0 \cos\alpha_0\} \,\mathrm{d}\xi \\ &+ \{[Q_\lambda \sin\theta_0 + H_\lambda \sin\theta_0 \cos\alpha_0] \sin\theta_0 \sin\alpha_0 \\ &+ [-Q_\lambda \tan\alpha_0 \sin\theta_0 - H_\lambda \sin\alpha_0 \sin\theta_0] \sin\theta_0 \cos\alpha_0\} \,\mathrm{d}\lambda \\ = &\ 0 \quad \text{as expected,} \end{aligned} \tag{A21}$$

$$\begin{aligned}\mathbf{i}_1 \cdot \mathrm{d}\mathbf{n}_0 = &\{G_\xi \sin\theta_0 + [-Q_\xi \sin\theta_0 + G_\xi \sin\alpha_0 \cot\theta_0] \cos\theta_0 \sin\alpha_0 \\ &+ [Q_\xi \tan\alpha_0 \sin\theta_0 + G_\xi \cos\alpha_0 \cot\theta_0] \cos\theta_0 \cos\alpha_0\} \,\mathrm{d}\xi \\ &+ \{-[Q_\lambda \sin\theta_0 + H_\lambda \sin\theta_0 \cos\alpha_0] \cos\theta_0 \sin\alpha_0 \\ &+ [Q_\lambda \tan\alpha_0 \sin\theta_0 + H_\lambda \sin\alpha_0 \sin\theta_0] \cos\theta_0 \cos\alpha_0\} \,\mathrm{d}\lambda \\ = &\ (1/\sin\theta_0)\, G_\xi \,\mathrm{d}\xi, \end{aligned} \tag{A22}$$

$$\begin{aligned}\mathbf{i}_2 \cdot \mathrm{d}\mathbf{n}_0 = &\{[Q_\xi \sin\theta_0 - G_\xi \cot\theta_0 \sin\alpha_0] \cos\alpha_0 \\ &+ [Q_\xi \sin\theta_0 \tan\alpha_0 + G_\xi \cot\theta_0 \cos\alpha_0] \sin\alpha_0\} \,\mathrm{d}\xi \\ &+ \{[Q_\lambda \sin\theta_0 + H_\lambda \sin\theta_0 \cos\alpha_0] \cos\alpha_0 \\ &+ [Q_\lambda \sin\theta_0 \tan\alpha_0 + H_\lambda \sin\theta_0 \sin\alpha_0] \sin\alpha_0\} \,\mathrm{d}\lambda \\ = &\ (\sin\theta_0/\cos\alpha_0)\, Q_\xi \,\mathrm{d}\xi + \sin\theta_0\, ((1/\cos\alpha_0)\, Q_\lambda + H_\lambda) \,\mathrm{d}\lambda. \end{aligned} \tag{A23}$$

13. We can now find the components, in the $\mathbf{i}_1$ and $\mathbf{i}_2$ directions, of the unit-vector increments $\boldsymbol{\varepsilon}$, $\boldsymbol{\varepsilon}'$ defined by equation (A20):

$$\varepsilon_1 = (1/\sin\theta_0)\, G_\xi \,\mathrm{d}\xi, \qquad \varepsilon_2 = (\sin\theta_0/\cos\alpha_0)\, Q_\xi \,\mathrm{d}\xi, \tag{A24}$$

$$\varepsilon'_1 = 0, \qquad \varepsilon'_2 = \sin\theta_0\, ((1/\cos\alpha_0)\, Q_\lambda + H_\lambda) \,\mathrm{d}\lambda. \tag{A25}$$

14. The next step is to find the cross-sectional area of the ray tube, $A(s)$, at an arbitrary distance $s$ from point B, measured along the reference ray.

Figure A2 shows the cross-section $\mathrm{C_0C_1C_2C_3}$ in $(x_1, x_2)$ co-ordinates, at $s = 0$. The dimensions $(f, g, h)$ of the parallelogram are given by

$$f = (\mathbf{i}_x \cdot \mathbf{i}_1)\, \mathrm{d}x_B(\mathrm{d}\xi, 0) = a \sin\theta_0\, X_\xi \,\mathrm{d}\xi, \tag{A26}$$

$$g = (\mathbf{i}_x \cdot \mathbf{i}_1)\, \mathrm{d}x_B(0, \mathrm{d}\lambda) = a \sin\theta_0\, X_\lambda \,\mathrm{d}\lambda, \tag{A27}$$

$$h = (\mathbf{i}_\phi \cdot \mathbf{i}_2)\, a\, \mathrm{d}\phi_B(0, \mathrm{d}\lambda) = a \cos\alpha_0\, H_\lambda \,\mathrm{d}\lambda, \tag{A28}$$

where we have used equations (A5), (A6), (A11) and (A13).

15. Further along the reference ray, the co-ordinates of $C_0, C_1, C_2, C_3$ change as follows:

| Point | $(x_1, x_2)$ at $s = 0$ | $(x_1, x_2)$ at arbitrary $s$ | |
|---|---|---|---|
| $C_0$ | 0, 0 | 0 | 0 |
| $C_1$ | $f, 0$ | $f + \varepsilon_1 s,$ | $\varepsilon_2 s$ |
| $C_2$ | $g, h$ | $g + \varepsilon'_1 s,$ | $h + \varepsilon'_2 s$ |
| $C_3$ | $f + g, h$ | $f + g + \varepsilon_1 s + \varepsilon'_1 s,$ | $h + \varepsilon_2 s + \varepsilon'_2 s$ |

The area of a triangle whose vertices are located at $[(0, 0), (a_1, a_2), (b_1, b_2)]$ is $\frac{1}{2}|a_1 b_2 - b_1 a_2|$. It follows that the ray-tube area at arbitrary $s$ is

$$A(s) = |fh + s(\varepsilon_1 h - \varepsilon_2 g + \varepsilon'_2 f) + s^2(\varepsilon_1 \varepsilon'_2 - \varepsilon_2 \varepsilon'_1)|. \tag{A29}$$

Note that the leading term gives the cross-sectional area at B (on the edge of the jet); while the $s^2$ term gives the farfield area, and accounts for spherical spreading.

16. The ray-tube area expression (A29) may be written as

$$A(s) = |A_0 + A_1 s + A_2 s^2|\,|\mathrm{d}\xi\,\mathrm{d}\lambda|. \tag{A30}$$

The coefficients follow, from equations (A24) to (A28). Thus

$$A_0 = a^2 \sin\theta_0 \cos\alpha_0 X_\xi H_\lambda, \tag{A31}$$

$$A_1 = \left\{\frac{1}{\sin\theta_0} a\cos\alpha_0 G_\xi H_\lambda - a\frac{\sin^2\theta_0}{\cos\alpha_0} Q_\xi X_\lambda + \alpha \sin^2\theta_0 \left(\frac{1}{\cos\alpha_0} Q_\lambda + H_\lambda\right) X_\xi\right\}, \tag{A32}$$

$$A_2 = \left(\frac{1}{\cos\alpha_0} Q_\lambda + H_\lambda\right) G_\xi. \tag{A33}$$

17. The explicit functions $G, H, Q, X$ and their derivatives are listed below. From equations (3), (4) and (13) of section 2

$$G(\xi, M, C) = \frac{\xi}{C(1 + M\xi)} \quad \left(C = \frac{c_1}{c_0};\ M = \frac{U}{c_1}\right), \tag{A34}$$

$$G_\xi = \frac{1}{C(1 + M\xi)^2} = \frac{C}{\xi^2} G^2, \tag{A35}$$

$$H\left(\lambda, \frac{r_s}{a}\right) = \lambda - \sin^{-1}(\sigma_s \sin\lambda) \qquad (\sigma_s = r_s/a), \tag{A36}$$

$$H_\lambda = 1 - \frac{\sigma_s \cos\lambda}{\sqrt{1 - \sigma_s^2 \sin^2\lambda}} = 1 - \beta_1. \tag{A37}$$

From equations (4), (6)–(8) and (12) of section 2,

$$Q(\xi, \lambda, M, C, \sigma_s) = \sin\alpha_0 = \left[\frac{(1 - \xi^2)}{(C^2(1 + M\xi)^2 - \xi^2)}\right]^{1/2} \sigma_s \sin\lambda, \tag{A38}$$

$$Q_\xi = \frac{[\xi - C^2(\xi + M)(1 + M\xi)]}{(1 - \xi^2)^{1/2}[C^2(1 + M\xi)^2 - \xi^2]^{3/2}} \sigma_s \sin\lambda, \tag{A39}$$

$$Q_\lambda = \left[\frac{(1 - \xi^2)}{(C^2(1 + M\xi)^2 - \xi^2)}\right]^{1/2} \sigma_s \cos\lambda = Q\cot\lambda. \tag{A40}$$

Finally, from equations (20), (13) and (18) of section 2,

$$X = \frac{d_1}{a}\frac{\xi + M}{\sqrt{1-\xi^2}},$$

$$X(\xi, \lambda, M, \sigma_s) = \frac{1}{\sin\lambda}\sin[\lambda - \sin^{-1}(\sigma_s \sin\lambda)]\frac{(\xi + M)}{\sqrt{1-\xi^2}}$$

$$= [(1 - \sigma_s^2 \sin^2\lambda)^{1/2} - \sigma_s \cos\lambda]\frac{(\xi + M)}{\sqrt{1-\xi^2}}, \tag{A41}$$

$$X_\xi = [(1 - \sigma_s^2 \sin^2\lambda)^{1/2} - \sigma_s \cos\lambda]\frac{(1 + M\xi)}{(1-\xi^2)^{3/2}}, \tag{A42}$$

$$X_\lambda = \left[\sigma_s \sin\lambda - \frac{\sigma_s^2 \sin\lambda\cos\lambda}{(1 - \sigma_s^2 \sin^2\lambda)^{1/2}}\right]\frac{(\xi + M)}{\sqrt{1-\xi^2}}. \tag{A43}$$

18. The ratio $\mathrm{d}A_n/\mathrm{d}\Omega_1$ which appears in equation (33) of section 2 can now be calculated as

$$\frac{\mathrm{d}A_n}{\mathrm{d}\Omega_1} = \frac{A(s)}{|\mathrm{d}\xi\,\mathrm{d}\lambda|} = |A_0 + A_1 s + A_2 s^2|, \tag{A44}$$

from equation (A30) above and equation (24) of section 2. The coefficients $A_0$, $A_1$, $A_2$ are known from paragraphs 16 and 17 above. The ray path length $s$ (equal to BM) is given by

$$s/a = 1/\sin\theta_0\,[\sqrt{\sigma_m^2 - \sin^2\alpha_0} - \cos\alpha_0] \qquad (\sigma_m = r_m/a) \tag{A45}$$

which follows from equation (29) of section 2 and the relation $s = d_0/\sin\theta_0$.

19. The following special cases of equation (A45) provide a useful check on the ray-tube area result, equation (A44).

(1) *Far field* ($\sigma_m \to \infty$):

$$s/a \approx \sigma_m/\sin\theta_0. \tag{A46}$$

(2) *Measurement on nozzle lip line* ($\sigma_m = 1$):

$$s/a = 0. \tag{A47}$$

(3) *Source on jet axis* ($\alpha_0 = 0$):

$$s/a = (1/\sin\theta_0)(\sigma_m - 1). \tag{A48}$$

We consider these special cases in turn, and evaluate equation (A44) for each one.

20. First, consider special case (1) which is analyzed independently in Appendix D. In the far field, equations (A44) and (A46) give

$$\frac{\mathrm{d}A_n}{\mathrm{d}\Omega_1} \approx |A_2|\frac{\sigma_m^2}{\sin^2\theta_0}a^2. \tag{A49}$$

With $A_2$ given by equations (A33, A35, A37, A40), we get

$$\frac{\mathrm{d}A_n}{\mathrm{d}\Omega_1} \approx \frac{r_m^2}{\sin^2\theta_0}\left|\frac{1}{\cos\alpha_0}\sin\alpha_0\cot\lambda + 1 - \beta_1\right|\frac{C}{\cos^2\theta_1}\cos^2\theta_0$$

$$= r_m^2 C\,\frac{\cos^2\theta_0}{\sin^2\theta_0}\,\frac{1}{\cos^2\theta_1}\,|1 - \beta_1 + \beta_0|. \tag{A50}$$

The quantities

$$\beta_1 = \partial\alpha_1/\partial\lambda = 1 - H_\lambda, \qquad \beta_0 = \partial\alpha_0/\partial\lambda = (1/\cos\alpha_0)\,Q_\lambda = \tan\alpha_0\cot\lambda \tag{A51, A52}$$

are introduced in Appendix D. Equation (A50) yields

$$\mathrm{d}A_m = \frac{1}{\sin\theta_0}\,\mathrm{d}A_n \quad \text{(see Figure 4)}$$

$$= r_m^2 C\,\frac{\cos^2\theta_0}{\sin^3\theta_0}\,\frac{|\mathrm{d}\xi\,\mathrm{d}\lambda|}{\cos^2\theta_1}\,|1 - \beta_1 + \beta_0|$$

$$= r_m^2 C\,\frac{\cos^2\theta_0}{\sin^3\theta_0}\,\frac{\sin\theta_1}{\cos^2\theta_1}\,|1 - \beta_1 + \beta_0||\mathrm{d}\lambda\,\mathrm{d}\theta_1|, \tag{A53}$$

which agrees with equation (D9)

21. Next, consider special case (2) which is analyzed independently in Appendix B. When $r_m = a$, $s = 0$ and equation (A44) gives

$$\mathrm{d}A_n/\mathrm{d}\Omega_1 = |A_0|$$

$$= a^2|\sin\theta_0\cos\alpha_0 X_\xi H_\lambda|$$

$$= a^2\left|\sin\theta_0\cos\alpha_0\,\frac{\sin\phi_B}{\sin\lambda}\,\frac{\cos\theta_1}{C\cos\theta_0}\,\frac{1}{\sin^3\theta_1}\,H_\lambda\right|; \tag{A54}$$

here we have used equation (A42) and converted the result back into the notation of Appendix B, using angles $\phi_B$ and $\theta_0$. Since

$$\mathrm{d}\Omega_1 = |\mathrm{d}\xi\,\mathrm{d}\lambda| = \sin\theta_1|\mathrm{d}\theta_1\,\mathrm{d}\lambda|, \tag{A55}$$

equation (A54) gives

$$\mathrm{d}A_n(r_m = a) = a^2 H_\lambda\cos\alpha_0\,\frac{\sin\phi_B}{\sin\lambda}\,\frac{\sin\theta_0}{C\cos\theta_0}\,\frac{\cos\theta_1}{\sin^2\theta_1}\,|\mathrm{d}\theta_1\,\mathrm{d}\lambda|. \tag{A56}$$

Equation (A56) agrees with Appendix B, equation (B7), where $H_\lambda$ is written as $F(\lambda)$. This provides a second check on our general result, equation (A44) above. The $A_0$ and $A_2$ terms have now both been verified, but we still need a check on $A_1$; a partial check is provided in the next two paragraphs, where we consider on-axis sources.

22. Our final check on equation (A44) is provided by special case (3) which is analyzed independently in Appendix C. When $r_s = 0$ (i.e., $\sigma_s = 0$), $\alpha_0$ becomes zero and the

coefficients $A_0$, $A_1$, $A_2$ simplify as follows:

$$H = \phi_B \to \lambda; \quad H_\xi = 0,\ H_\lambda = 1, \tag{A57}$$

$$Q = \sin\alpha_0 \to 0; \quad Q_\xi = 0,\ Q_\lambda = 0, \tag{A58}$$

$$X \to \frac{(\xi + M)}{\sqrt{1-\xi^2}} \qquad (\text{since } d_1 \to a),$$

$$X_\xi = \frac{(1+M\xi)}{(1-\xi^2)^{3/2}} = \frac{\cos\theta_1}{C\cos\theta_0}\frac{1}{\sin^3\theta_1}, \quad X_\lambda = 0. \tag{A59}$$

Thus

$$A_0 = a^2 \sin\theta_0 \frac{1}{C\cos\theta_0}\frac{\cos\theta_1}{\sin^3\theta_1}, \tag{A60}$$

$$A_1 = aC\frac{\cos^2\theta_0}{\cos^2\theta_1}\frac{1}{\sin\theta_0} + a\sin^2\theta_0\frac{1}{C\cos\theta_0}\frac{\cos\theta_1}{\sin^3\theta_1}, \tag{A61}$$

$$A_2 = C\frac{\cos^2\theta_0}{\cos^2\theta_1}. \tag{A62}$$

23. The ray path length $s$ in this case is given by equation (48) as $s = (r_m - a)/\sin\theta_0$. Substituting equations (A60)–(A62) in equation (A44) gives, for on-axis sources,

$$\begin{aligned}\frac{1}{a^2}\frac{\mathrm{d}A_n}{\mathrm{d}\Omega_1} = \Bigg|&\frac{1}{C}\tan\theta_0\frac{\cos\theta_1}{\sin^3\theta_1} \\ &+ \left(\frac{r_m}{a}-1\right)\left(C\cot^2\theta_0\frac{1}{\cos^2\theta_1} + \frac{1}{C}\tan\theta_0\frac{\cos\theta_1}{\sin^3\theta_1}\right) \\ &+ \left(\frac{r_m}{a}-1\right)^2 C\cot^2\theta_0\frac{1}{\cos^2\theta_1}\Bigg|.\end{aligned} \tag{A63}$$

The constant terms (i.e., those independent of $r_m$) on the right side cancel, leaving

$$\begin{aligned}\frac{1}{a^2}\frac{\mathrm{d}A_n}{\mathrm{d}\Omega_1} &= \left|\left(\frac{r_m}{a}\right)^2 C\cot^2\theta_0\frac{1}{\cos^2\theta_1} + \left(\frac{r_m}{a}\right)\left(\frac{1}{C}\tan\theta_0\frac{\cos\theta_1}{\sin^3\theta_1} - C\cot^2\theta_0\frac{1}{\cos^2\theta_1}\right)\right| \\ &= C\cot^2\theta_0\frac{1}{\cos^2\theta_1}\left|\left(\frac{r_m}{a}\right)^2 + \left(\frac{r_m}{a}\right)\left\{\frac{1}{C^2}\left(\frac{\tan\theta_0}{\tan\theta_1}\right)^3 - 1\right\}\right|,\end{aligned} \tag{A64}$$

which agrees with the result in equation (C4).

24. All three special cases listed in paragraph 19 above have now been checked; in each case the general result, equation (A44), agrees with the independent analyses of Appendices B, C, and D. The only terms not checked in this process are the $Q_\xi$ and $Q_\lambda$ terms in equation (A32). We have therefore based the numerical study of Section 4 on equation (A44), with the three coefficients ($A_0$, $A_1$, $A_2$) given by equations (A31)–(A43).

## APPENDIX B. SIMPLIFIED EXACT ANALYSIS OF RAY-TUBE AREA: (i) MEASUREMENTS IMMEDIATELY OUTSIDE JET SHEAR LAYER

It is straightforward to calculate $\mathrm{d}A_n$ exactly for points immediately outside the shear layer ($r_m = a$), noting that $\mathrm{d}A_n$ is then related to $\mathrm{d}A_m$ by $\mathrm{d}A_n = \mathrm{d}A_m\, n_{0r} = \mathrm{d}A_m \sin\theta_0 \cos\alpha_0$.

The area $A_m$ on the cylinder $r = r_m$ is given, for the special case $r_m = a$, by

$$\mathrm{d}A_m = a|\mathrm{d}\phi_B\,\mathrm{d}x_B|, \tag{B1}$$

where

$$\mathrm{d}\phi_B = (\partial\phi_B/\partial\lambda)_{\theta_1}\,\mathrm{d}\lambda, \qquad \mathrm{d}x_B = (\partial x_B/\partial\theta_1)_\lambda\,\mathrm{d}\theta_1 \tag{B2}$$

and $\phi_B$, $x_B$ are given by equations (13), (20) and (18). It follows that

$$\mathrm{d}\phi_B = \left\{1 - \frac{(r_s/a)\cos\lambda}{\sqrt{1 - ((r_s/a)\sin\lambda)^2}}\right\}\mathrm{d}\lambda = F(\lambda)\,\mathrm{d}\lambda \quad \text{(say)}, \tag{B3}$$

$$\mathrm{d}x_B = -\,a\,\frac{\sin\phi_B}{\sin\lambda}\,\frac{(1 + (U/c_1)\cos\theta_1)}{\sin^2\theta_1}\,\mathrm{d}\theta_1. \tag{B4}$$

Finally, substituting equations (B3) and (B4) in equation (B1) gives

$$\mathrm{d}A_m = a^2\,F(\lambda)\,\frac{\sin\phi_B}{\sin\lambda}\,\frac{\mathrm{d}\lambda\,\mathrm{d}\theta_1}{D_1\sin^2\theta_1}. \tag{B5}$$

The ray-tube area $\mathrm{d}A_n\,(= \mathrm{d}A_m\sin\theta_0\cos\alpha_0)$ follows directly. We can now combine equation (B5) with the $\phi_B$ equation (13) and the $\alpha_0$ equation

$$\sin^2\alpha_0 = \frac{\sin^2\theta_1}{(E^{-2} - \cos^2\theta_1)}\left(\frac{r_s}{a}\right)^2\sin^2\lambda \tag{B6}$$

—which follows from equations (8), (9) and (12)—to obtain the exact ray-tube area at point B immediately outside the shear layer. For comparison purposes, we write the exact result at $r_m = a$ as

$$\frac{\mathrm{d}A_n}{r_m^2} = F(\lambda)\,\frac{\sin\phi_B}{\sin\lambda}\cos\alpha_0\,\frac{c_0}{c_1}\,\frac{\sin\theta_0}{\cos\theta_0}\,\frac{\cos\theta_1}{\sin^2\theta_1}\,|\mathrm{d}\lambda\,\mathrm{d}\theta_1|. \tag{B7}$$

The first three factors on the right of equation (B7) are equal to 1 for on-axis sources; this fact is used below in Appendix C, to provide a cross-check on equation (B7). The form of equation (B7) also allows direct comparison with the approximate ray-tube area expression given in equation (38) of section 3.2, and with the exact general expression derived in Appendix A.

## APPENDIX C. SIMPLIFIED EXACT ANALYSIS OF RAY-TUBE AREA: (ii) SOURCE ON JET AXIS

A second check on the exact expression for $\mathrm{d}A_n$ derived in Appendix A can be found by locating the source on the jet axis; the result obtained below places no restriction on the measurement radius, beyond $r_m > a$. The ray-tube area is given exactly in this case by

$$\mathrm{d}A_n = R_{r0}(R_{r0} + \Delta R_r)\sin\theta_0|\mathrm{d}\theta_0\,\mathrm{d}\lambda|, \tag{C1}$$

where $\Delta R_r$ is defined in Figure A5. From equation (29) of reference [1],

$$\Delta R_r = (a/\sin\theta_0)\,[(\tan\theta_0/\tan\theta_1)^3\,(c_0/c_1)^2 - 1]. \tag{C2}$$

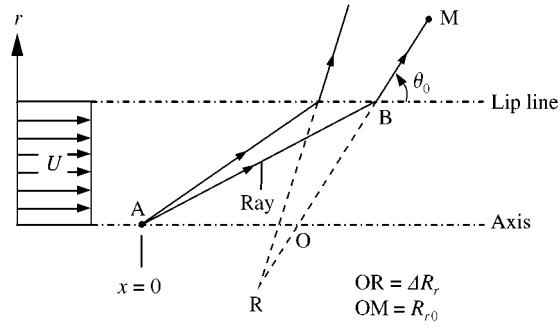


Figure A5. Near-field correction for a source on the jet axis.

Equation (D6) of Appendix D gives

$$\sin\theta_0\,\mathrm{d}\theta_0 = \frac{c_1}{c_0}\frac{\cos^2\theta_0}{\cos^2\theta_1}\sin\theta_1\,\mathrm{d}\theta_1 \tag{C3}$$

and $R_{r0}$ is defined by equation (36). Combining these results gives

$$\frac{\mathrm{d}A_n}{r_m^2} = \left\{1 + \frac{a}{r_m}\left[\left(\frac{\tan\theta_0}{\tan\theta_1}\right)^3\left(\frac{c_0}{c_1}\right)^2 - 1\right]\right\}\frac{c_1\cos^2\theta_0}{c_0\sin^2\theta_0}\frac{\sin\theta_1}{\cos^2\theta_1}\,\mathrm{d}\lambda\,\mathrm{d}\theta_1 \tag{C4}$$

which gives $\mathrm{d}A_n$ exactly for on-axis sources.

A corresponding approximate expression is obtained from equation (38), section 3.2.2:

$$\frac{\mathrm{d}A_n}{r_m^2} \approx \frac{c_1}{c_0}\frac{\cos^2\theta_0}{\sin^2\theta_0}\frac{\sin\theta_1}{\cos^2\theta_1}\,\mathrm{d}\lambda\,\mathrm{d}\theta_1. \tag{C5}$$

For on-axis sources, the only difference between the exact expression, equation (C4), and the approximation above is the factor in curly brackets. This observation suggests that the more general approximate expression in equation (38) could be improved simply by inserting the curly-bracketed factor from equation (C4).

In the special case $r_m = a$ considered in Appendix B, this bracketed factor takes the value

$$\{\cdots\} = \left(\frac{\tan\theta_0}{\tan\theta_1}\right)^3\left(\frac{c_0}{c_1}\right)^2. \tag{C6}$$

Therefore, for a combination of (i) measurement position immediately outside the shear layer and (ii) on-axis sources,

$$\frac{\mathrm{d}A_n}{r_m^2} = \frac{c_0}{c_1}\frac{\sin\theta_0}{\cos\theta_0}\frac{\cos\theta_1}{\sin^2\theta_1}\,\mathrm{d}\lambda\,\mathrm{d}\theta_1. \tag{C7}$$

This special case of equation (C4) agrees exactly with the on-axis version of equation (B7), which was derived for any source position and $r_m = a$.

## APPENDIX D: RAY-TUBE AREA CALCULATION IN THE FAR FIELD

The area $\mathrm{d}A_m$, defined in Figure 4, has a farfield asymptotic value

$$\mathrm{d}A_m \approx r_m|\mathrm{d}\phi_0\,\mathrm{d}x_0|, \tag{D1}$$

where

$$\mathrm{d}\phi_0 = \left.\frac{\partial \phi_0}{\partial \lambda}\right|_{\theta_1} \mathrm{d}\lambda, \qquad \mathrm{d}x_0 = \left.\frac{\partial x_0}{\partial \theta_1}\right|_{\lambda} \mathrm{d}\theta_1; \tag{D2, D3}$$

the farfield azimuthal angle $\phi_0$ is given by equation (21) of section 2.4 for finite $r_s/a$, and the farfield axial ray displacement $x_0$ is

$$x_0 = r_m \cot \theta_0. \tag{D4}$$

Thus

$$\left.\frac{\partial x_0}{\partial \theta_1}\right|_{\lambda} = -\frac{r_m}{\sin^2 \theta_0} \frac{\mathrm{d}\theta_0}{\mathrm{d}\theta_1}, \tag{D5}$$

where $\mathrm{d}\theta_0/\mathrm{d}\theta_1$ follows from the differential version of equation (3):

$$c_0 \frac{\sin \theta_0}{\cos^2 \theta_0} \mathrm{d}\theta_0 = c_1 \frac{\sin \theta_1}{\cos^2 \theta_1} \mathrm{d}\theta_1. \tag{D6}$$

Combining the last two equations gives

$$\left.\frac{\partial x_0}{\partial \theta_1}\right|_{\lambda} = -r_m \frac{c_1}{c_0} \frac{\cos^2 \theta_0}{\sin^3 \theta_0} \frac{\sin \theta_1}{\cos^2 \theta_1}. \tag{D7}$$

Also, since $K_1/K_0$ depends on $\theta_1$ but not on $\lambda$ (as equation (9) demonstrates), differentiating equation (21) gives

$$\begin{aligned} \left.\frac{\partial \phi_0}{\partial \lambda}\right|_{\theta_1} &= 1 - \left[1 - \left(\frac{r_s}{a}\right)^2 \sin^2 \lambda\right]^{-1/2} \frac{r_s}{a} \cos \lambda + \left[1 - \left(\frac{K_1}{K_0}\right)^2 \left(\frac{r_s}{a}\right)^2 \sin^2 \lambda\right]^{-1/2} \frac{K_1}{K_0} \frac{r_s}{a} \cos \lambda \\ &= 1 - \beta_1 + \beta_0, \end{aligned} \tag{D8}$$

where $\beta_1 = \partial \alpha_1/\partial \lambda$ and $\beta_0 = \partial \alpha_0/\partial \lambda$.

It follows from these results that in the far field ($r_m/a \to \infty$),

$$\begin{aligned} \mathrm{d}A_m &\approx r_m^2 \frac{c_1}{c_0} \frac{\cos^2 \theta_0}{\sin^3 \theta_0} \frac{\sin \theta_1}{\cos^2 \theta_1} |1 - \beta_1 + \beta_0| \, |\mathrm{d}\lambda \, \mathrm{d}\theta_1| \\ &\approx \frac{r_m^2}{\sin \theta_0} |1 - \beta_1 + \beta_0| \frac{c_1}{c_0} \frac{E^2 \sin \theta_1}{1 - E^2 \cos^2 \theta_1} |\mathrm{d}\lambda \, \mathrm{d}\theta_1|. \end{aligned} \tag{D9}$$

In equation (D9), the relation $\cos \theta_0 = E \cos \theta_1$ from equation (15) has been used to replace $\theta_0$ by $\theta_1$.

## APPENDIX E: NOMENCLATURE

| | |
|---|---|
| $a$ | flight-stream nozzle radius |
| $A(s)$ | cross-sectional area of ray tube formed by the four rays through points $B_0$, $B_1$, $B_2$, $B_3$ |
| $A_0$, $A_1$, $A_2$ | coefficients in $A(s)$ expression |
| $\mathrm{d}A_m$ | ray-tube area on measurement cylinder, $r = r_m$ |
| $\mathrm{d}A_n$ | ray-tube cross-sectional area at measurement position |
| $c_1$, $c_0$ | sound speed inside, outside jet |
| $C$ | ratio of sound speeds $c_1/c_0$ |
| $d_1$ | distance in transverse plane between A and B |
| $d_0$ | distance in transverse plane between B and M |

| | |
|---|---|
| $D_1$ | Doppler factor $\omega_1/\omega_0$, defined in equation (4) |
| $E$ | $\cos\theta_0/\cos\theta_1 = (c_0/c_1)D_1$ |
| $f, f'$ | base-lengths of parallelograms $C_0C_1C_2C_3$, $B_0B_1B_2B_3$; see equation (A2) |
| $F(\lambda)$ | function of azimuthal ray launch angle $\lambda$, defined in equation (B3) |
| $g, g'$ | offsets of parallelograms $C_0C_1C_2C_3$, $B_0B_1B_2B_3$ |
| $G$ | $\cos\theta_0$ |
| $h, h'$ | heights of parallelograms $C_0C_1C_2C_3$, $B_0B_1B_2B_3$ |
| $H$ | $\phi_B$ |
| $\mathbf{i}_x, \mathbf{i}_r, \mathbf{i}_\phi$ | set of orthogonal unit vectors based on co-ordinate directions at B |
| $\mathbf{i}_1, \mathbf{i}_2$ | orthogonal unit vectors, normal to $\mathbf{n}_0$ |
| $k_x$ | axial wavenumber |
| $k_1, k_0$ | acoustic wavenumbers, $\omega_1/c_1$, $\omega_0/c_0$ |
| $K_1, K_0$ | wavenumbers in transverse plane, for waves propagating inside and outside the flow respectively |
| $M$ | flight stream Mach number, $U/c_1$ |
| $\mathbf{n}_1, \mathbf{n}_0$ | unit wavenormal vectors inside, outside jet |
| $P_m$ | power spectrum of acoustic pressure at measurement position M |
| $P_\infty$ | power spectrum of acoustic pressure under farfield flight conditions |
| $Q$ | $\sin\alpha_0$ |
| $r$ | radius from jet axis |
| $r_m$ | measurement radius outside jet |
| $r_s$ | radial position of source |
| $R_r$ | wavefront propagation distance from source, relative to fluid |
| $\Delta R_r$ | correction to propagation distance |
| $R_{r0}$ | distance OM, Figure A5 |
| $R_{r\infty}$ | farfield value of $R_r$ for aircraft in flight |
| $s$ | distance measured from B along ray |
| $U$ | jet flow velocity |
| $v_t, v_x$ | components of $\mathbf{v}$ transverse and parallel to jet axis |
| $\mathbf{v}$ | ray velocity |
| $dW_1, dW_0$ | sound power in ray tube inside, outside jet |
| $x$ | axial co-ordinate (with source at $x = 0$) |
| $x_B$ | axial co-ordinate of point where ray crosses shear layer |
| $x_m$ | axial co-ordinate of measurement position |
| $x_1, x_2$ | co-ordinates in plane normal to reference ray outside jet, with origin on the ray (at $C_0$) |
| $X$ | $x_B/a$ |
| $\alpha_1, \alpha_0$ | ray or wavenormal angles in plane transverse to jet axis, relative to radial direction at B (i.e., angles of incidence and transmission respectively) |
| $\beta_1, \beta_0$ | $\partial\alpha_1/\partial\lambda$, $\partial\alpha_0/\partial\lambda$ |
| $\delta$ | angle related to near-field geometry, Figure 7 |
| $\boldsymbol{\varepsilon}, \boldsymbol{\varepsilon}'$ | increments in $\mathbf{n}_0$ |
| $\varepsilon_1, \varepsilon_2; \varepsilon_1', \varepsilon_2'$ | components of $\boldsymbol{\varepsilon}$ or $\boldsymbol{\varepsilon}'$ parallel to $\mathbf{i}_1, \mathbf{i}_2$ |
| $\xi$ | $\cos\theta_1$ |
| $\theta_1, \theta_0$ | wavenormal polar angles relative to jet axis, inside and outside the flow respectively |
| $\lambda$ | azimuthal launch angle for ray leaving source |
| $\rho_1, \rho_0$ | fluid density inside and outside the jet |
| $\sigma$ | dimensionless radial co-ordinate $r/a$ |
| $\phi$ | azimuthal angle about jet axis, defined so that source is at $\phi = 0$ |
| $\phi_B$ | azimuthal position of point B where ray crosses shear layer |
| $\phi_m$ | azimuthal position of measurement point outside shear layer |
| $\phi_0$ | azimuthal orientation of emerging ray |
| $\omega, \omega_0$ | angular frequency in a reference frame which is fixed with respect to the laboratory (or the aircraft) |
| $\omega_1$ | angular frequency in a reference frame which is fixed with respect to the flight-simulation jet flow (or the atmosphere) |
| $\Omega$ | solid angle |
| $d\Omega_1$ | solid angle formed by a small cone of wavenormal directions leaving the source, inside the jet |
| $d\Omega_0$ | solid angle formed by the corresponding rays in the far field, outside the flow |

Subscripts

| | |
|---|---|
| $B$ | position B |
| $m$ | measurement position M |
| $r$ | radial component of vector |
| $s$ | source position |
| $t$ | transverse component of vector |
| $x$ | axial component of vector |
| $\phi$ | azimuthal component of vector |
| $\lambda, \xi$ | partial derivatives with respect to $\lambda$ or $\xi$ |
| 1 | value inside jet |
| 0 | value outside jet |
| $\infty$ | value in farfield |